ACS NANO
Cite This: ACS Nano 2017, 11, 10591-10598
www.acsnano.org
ARTICLE

Rheotaxis of Bimetallic Micromotors Driven by Chemical–Acoustic Hybrid Power

Liqiang Ren,[†] Dekai Zhou,[‡] Zhangming Mao,[†] Pengtao Xu,[§] Tony Jun Huang,[∥] and Thomas E. Mallouk*[,†,§,⊥]

[†]Department of Engineering Science and Mechanics, [§]Department of Chemistry, and [⊥]Department of Biochemistry and Molecular Biology and Department of Physics, The Pennsylvania State University, University Park, Pennsylvania 16802, United States

[‡]School of Mechatronics Engineering, Harbin Institute of Technology, Harbin 150001, China

[∥]Department of Mechanical Engineering and Material Science, Duke University, Durham, North Carolina 27708, United States

Supporting Information

ABSTRACT: **Rheotaxis is a common phenomenon in nature that refers to the directed movement of microorganisms as a result of shear flow. The ability to mimic natural rheotaxis using synthetic micro/nanomotors adds functionality to enable their applications in biomedicine and chemistry. Here, we present a hybrid strategy that can achieve both positive and negative rheotaxis of synthetic bimetallic micromotors by employing a combination of chemical fuel and acoustic force. An acoustofluidic device is developed for the integration of the two propulsion mechanisms. Using acoustic force alone, bimetallic microrods are propelled along the bottom surface in the center of a fluid channel. The leading end of the microrod is always the less dense end, as established in earlier experiments. With chemical fuel (H_2O_2) alone, the microrods orient themselves with their anode end against the flow when shear flow is present. Numerical simulations confirm that this orientation results from tilting of the microrods relative to the bottom surface of the channel, which is caused by catalytically driven electro-osmotic flow. By combining this catalytic orientation effect with more powerful, density-dependent acoustic propulsion, both positive and negative rheotaxis can be achieved. The ability to respond to flow stimuli and collectively propel synthetic microswimmers in a directed manner indicates an important step toward practical applications.**

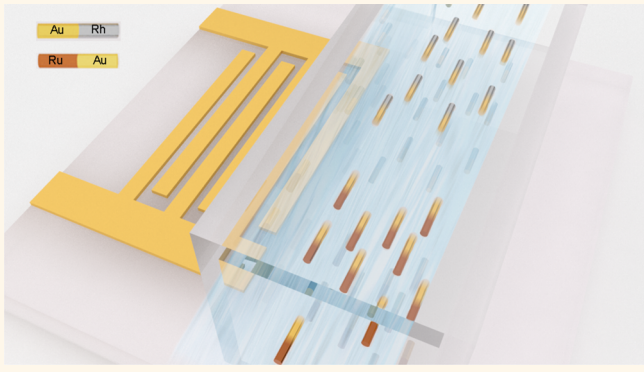

KEYWORDS: *synthetic micro/nanomotor, rheotaxis, acoustic propulsion, chemical propulsion, acoustofluidics*

Synthetic, autonomous micro/nanomotors have attracted tremendous attention since they were first demonstrated by Paxton *et al.*[1] These tiny devices, which move autonomously in fluids by harvesting energy from surrounding or on-board chemical fuel[2] or from external fields (acoustic, magnetic, electric, and electromagnetic)[3] can mimic the behavior of natural micro-organisms in several ways. Their biomimetic behavior increases our fundamental understanding of microscopic motility and also suggests applications ranging from biomedicine to environmental chemistry.[4−7] Over the past decade, synthetic micromotors of different shapes and propulsion mechanisms have been fabricated and investigated. Based on their specific properties, a number of functions such as cargo loading and unloading,[8−10] guided movement,[11−14] and drilling of biomaterial[15] have been demonstrated. Synthetic micromotors also exhibit biomimetic collective behaviors such as swarming and predator−prey responses.[16−19] However, most studies have been done in a closed, static fluid environment, which is highly restrictive for *in vitro* or *in vivo* practical applications. The response and behavior of the synthetic micromotors in dynamic environments such as shear flow have only recently begun to be explored.[20]

Shear flow is ubiquitous in nature and in applications of biomedicine. For example, laminar shear flow is the normal condition for blood throughout most of the circulatory system, and many bioanalytical methods, such as immunoassay, depend on flow. The study of synthetic micromotor behavior in shear flow thus could have far-reaching impact for biomedical applications. In response to shear flow, many micro-organisms change their movement patterns and align themselves along or against the direction of flow, especially when they are near surfaces. This effect is referred to as rheotaxis.[21−23] One famous

Received: August 27, 2017
Accepted: September 13, 2017
Published: September 13, 2017

DOI: 10.1021/acsnano.7b06107
ACS Nano 2017, 11, 10591−10598

example is the continuous upstream movement of spermatozoa (positive rheotaxis), which is considered as the main mechanism for sperm cells reaching the egg cell in natural fertilization.[24] Recently, synthetic microswimmers that can navigate upstream have been reported. Palacci *et al.* designed self-diffusiophoretic hematite particles that interact with solid surfaces through osmotic flow and polarize their catalytic end toward the surface. In shear flow, these swimmers experience a viscous torque because of the polarization and exhibit positive rheotaxis.[25] Self-diffusiophoresis Janus spheres were also reported to interact with surfaces or boundaries,[26,27] and their rheotaxis was theoretically predicted.[28] To date, only one-directional (positive) rheotaxis has been demonstrated by synthetic micromotors. The upstream movement requires a flow velocity that is slower than motor speed, and the rheotaxis of chemically propelled microswimmers can be exploited only in moderate flow due their limited speed (usually less than 50 μm/s[29]). In addition, the fuels used for fast chemical propulsion are often toxic, especially at high concentration. The low-energy conversion efficiency and toxicity associated with chemical micromotors are thus limiting in terms of their ultimate applications.

In contrast to chemical propulsion, acoustic propulsion is noninvasive, fuel-free, salt-tolerant, and relatively efficient. Bimetallic micromotors have been propelled at axial speeds of 200 μm/s using acoustic power levels that are safe for *in vivo* imaging.[30−32] The combination of chemical and acoustic propulsion has also opened up an approach for manipulation and functionalization of bimetallic micromotors. Individual and collective behaviors resulting from dual propulsions in opposite directions have been demonstrated.[33,34] Despite these interesting findings, it has been difficult to integrate acoustic propulsion with shear flow or to develop applications based on chemical−acoustic hybrid propulsion. Experimental and theoretical studies have suggested that an acoustic resonant chamber is required in order to propel the autonomous motion of micromotors.[35,36] For this reason, almost all studies of acoustic propulsion of bimetallic micromotors have been done in the levitation plane of thin film fluidic chambers.[30] The micromotors, along with cells and other particles with which they interact, are suspended at the midplane of the chamber and thus experience negligible shear flow. In addition to autonomous axial movement, organization into spinning chains, orbital motion, and aggregation are observed simultaneously.[30] The complex nodal pattern in the levitation plane makes it difficult to generate predictable and controllable movement, and external forces such as magnetic fields are needed to guide the movement of the micromotors. Finally, the density mismatch between bimetallic micromotors and the medium typically leads to motion near the bottom surface in chemical propulsion. Micromotors that exhibit unique behavior in the chemical field near the bottom surface would have to travel a long distance without reorienting in order to reach the levitation plane, where they can be driven by acoustic propulsion.

On the other hand, the study of acoustofluidics that explores acoustic behavior in microfluidic systems has been well-established.[37,38] Various acoustic resonant patterns have been designed and employed for three-dimensional (3D) patterning, transport, rotation, and alignment of cells/particles.[39−42] Here, we present an acoustofluidic device in which bimetallic micromotors can be propelled near a surface by acoustic force, chemical force, or both. With the acoustic field alone, the bimetallic micromotors are aligned with the pressure node in the fluid channel and bidirectionally propelled along the node. With chemical fuel alone, the micromotors are oriented by shear flow near the surface, consistent with numerical simulations of the chemically driven fluid flow. By combining the orientation effect of chemical propulsion and the directional propulsion by the acoustic field, both positive and negative rheotaxis are demonstrated, with the sign determined by the structure of the bimetallic micromotors. The strength of acoustic propulsion enables this effect to be observed in relatively fast flows, a desirable property for *in vivo* and *in vitro* applications.

RESULTS AND DISCUSSION

Design of the Acoustofluidic Device. As shown in Figure 1a (Figure S1), the acoustofluidic device contains a surface

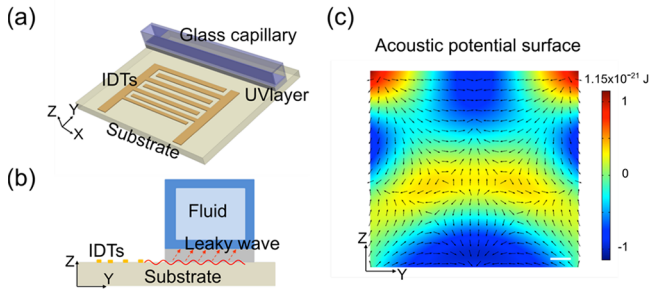

Figure 1. (a) Schematic of the acoustofluidic device and (b) illustration of its working mechanism. A surface acoustic wave is coupled into a square capillary through leaky wave generated in the coupling layer. (c) Cross-sectional view of the simulated acoustic potential profile. The scale bar is 20 μm.

acoustic wave (SAW) generator, which is a lithium niobate ($LiNbO_3$) substrate with chirped interdigital transducers (IDTs) deposited on it and a square glass capillary. The two parts were bonded and coupled to each other by a 60 μm thick ultraviolet (UV) epoxy layer. The ends of the glass capillary were connected to silicone tubing to enable injection of the bimetallic micromotor suspension. The chirped IDTs were designed to work between 3 and 7 MHz. We employed a SAW generator as the acoustic source because it shows better uniformity of wavefronts and wider working bandwidth than a bulk acoustic wave transducer.[43] In the experiment, the SAW is generated by applying a radio frequency signal to the IDTs and then propagates along the *Y* direction. As shown in Figure 1b, when the SAW encounters the UV epoxy coupling layer, a longitudinal leaky wave that propagates from the substrate into the glass capillary is generated, leading to vibration transmitted from the substrate to the glass capillary. Depending on the frequency of the SAW, various resonant modes can be formed in the glass capillary.

The acoustic field in the glass capillary was numerically simulated by modification of a COMSOL model developed in ref 44. Specifically, a two-dimensional (2D) model consisting of an epoxy layer, a square glass capillary, and fluid in the capillary (Figure S2) was built in the acoustic−solid interaction module to simulate the cross section of the acoustofluidic device. The surface acoustic wave was introduced into the model by adding the SAW displacements to the bottom boundary of the epoxy layer. We solved the first-order wave equation in the frequency domain to obtain the acoustic field in the fluid. Then the

DOI: 10.1021/acsnano.7b06107
ACS Nano 2017, 11, 10591−10598

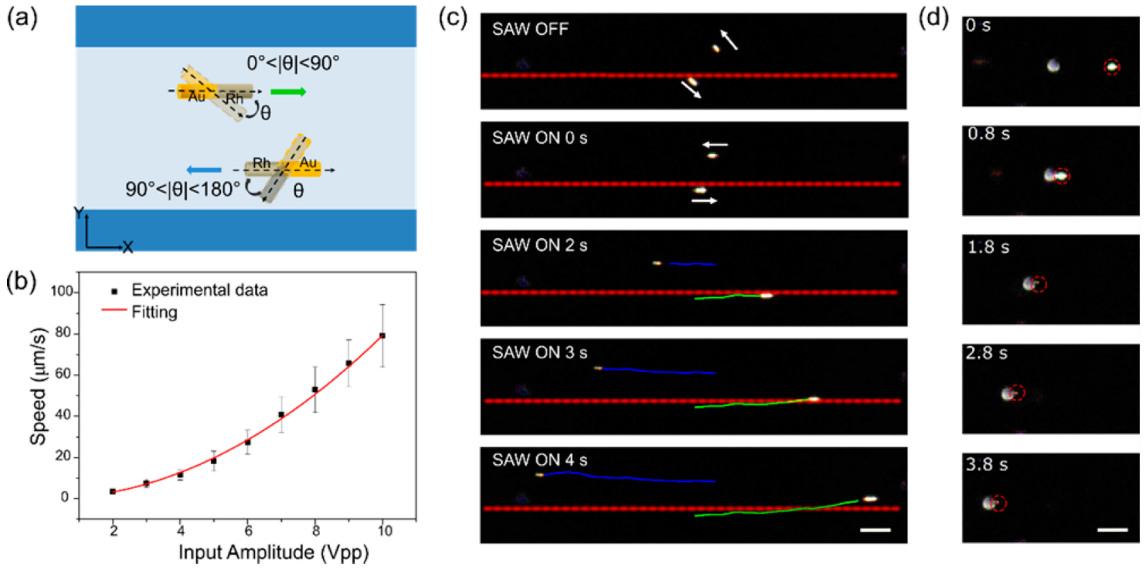

Figure 2. (a) Schematic illustration of the two polarizations of bimetallic motors in the acoustofluidic device. (b) Axial velocity of motors is proportional to the square of the driven voltage $V_{p\text{-}p}$. (c) Demonstration of bidirectional motion of two motors that have different initial θ. The Rh end is darker than the Au end in the dark-field mode of the microscope. (d) Transport of 4 μm SiO_2 particles by the bimetallic motor. The motor is indicated by the red dashed circle. The scale bar is 10 μm.

acoustic potential and radiation force were calculated according to Gor'kov's expression.[45] For simplicity, we approximated the micromotors to be metal spheres with a diameter of 300 nm. More detailed information about the simulations can be found in the Supporting Information.

Figure 1c shows a cross-sectional view of the simulated acoustic potential profile in the glass capillary (400 × 400 μm outer dimensions and 200 × 200 μm inner dimensions). The normalized arrows indicate the local direction of the acoustic radiation force on the micromotors. Although there are multiple pressure nodes (the potential minimum positions) that form along the entire cross section, almost all of the micromotors should be confined to the bottom center region of the capillary because of their initial near-bottom position. Theoretically there is no constraint in the X direction, and micromotors should be free to move autonomously along the X axis. The frequency of the SAW for the simulation was 5.42 MHz, the value used in later experiments. The simulation results were validated by patterning silica tracer particles (Figure S3), which rapidly localized to the bottom surface along the center line.

Bidirectional Motion of Acoustically Propelled Bimetallic Micromotors. As expected, the bimetallic micromotors exhibited distinct autonomous motion in the glass capillary. Au−Rh bimetallic rods (2−3 μm in length and 300 nm in diameter) were fabricated by template-assisted electrochemical deposition and suspended in deionized (DI) water. The micromotors are driven to the bottom of the capillary by gravity within several seconds of their injection into the capillary by a syringe. They show random Brownian motion at the bottom of the capillary when there is no SAW. When we turn the SAW on, all the micromotors align their long axis to the pressure node line (X axis) on a short time scale (less than 0.033 s). The asymmetry of bimetallic micromotors leads to two kinds of orientations, with the Rh end heading in the $+X$ or $-X$ direction. The orientation is determined by the initial angle between the long axis of the rod and the X axis, θ, at the moment that the SAW is turned on. As shown in Figure 2a, the Rh end heads in the $+X$ direction if $0° \leq |\theta| \leq 90°$, and otherwise, the Rh end heads in the $-X$ direction. Interestingly, the alignment is insensitive to the initial Y position of micromotors, even if they are far from the pressure node in the Y direction. With their long axis locked in the direction of the pressure node line, the bimetallic micromotors start to move autonomously with their Rh ends leading. The speed of axial motion V_x was proportional to the square of the applied voltage (Figure 2b). Both the moving direction and velocity are consistent with the acoustic streaming propulsion mechanism previously described for micromotors driven by excitation in the Z direction.[35,32] The trajectory of each micromotor could be continuously tracked under the microscope. No significant shift in the Z direction could be observed using a 20× objective, indicating that the micromotors are moving near the bottom surface. By controlling the timing of turning the SAW on and off, individual micromotors could be driven forward and in reverse (Movie S1). With multiple micromotors present, propulsion in both the $+X$ and $-X$ direction was observed simultaneously. Figure 2c (Movie S2) demonstrates that two micromotors with different initial θ angles are propelled in opposite directions. The red dashed line indicates the center line of the pressure node.

The directional propulsion of the micromotors is controllable and can be adapted to cargo transport. The micromotors and tracer particles (used to model cargo here) are confined to the pressure node, so the micromotors can pick up their cargo easily. As shown in Figure 2d (Movie S3), a Rh−Au rod was propelled toward a stationary silica tracer particle and pushed it forward after the collision. No chemical or biological surface modification was required for the pick-up process.

According to the simulated acoustic field, the bimetallic micromotors should also experience a force F_y that pushes them toward the pressure node line in the Y direction. However, this force is relatively weak because of the small radius of the micromotors, and it decreases dramatically as the micromotors approach the center of the pressure node (Figure S4). In addition, the drag force induced by acoustic streaming, which is

DOI: 10.1021/acsnano.7b06107
ACS Nano 2017, 11, 10591−10598

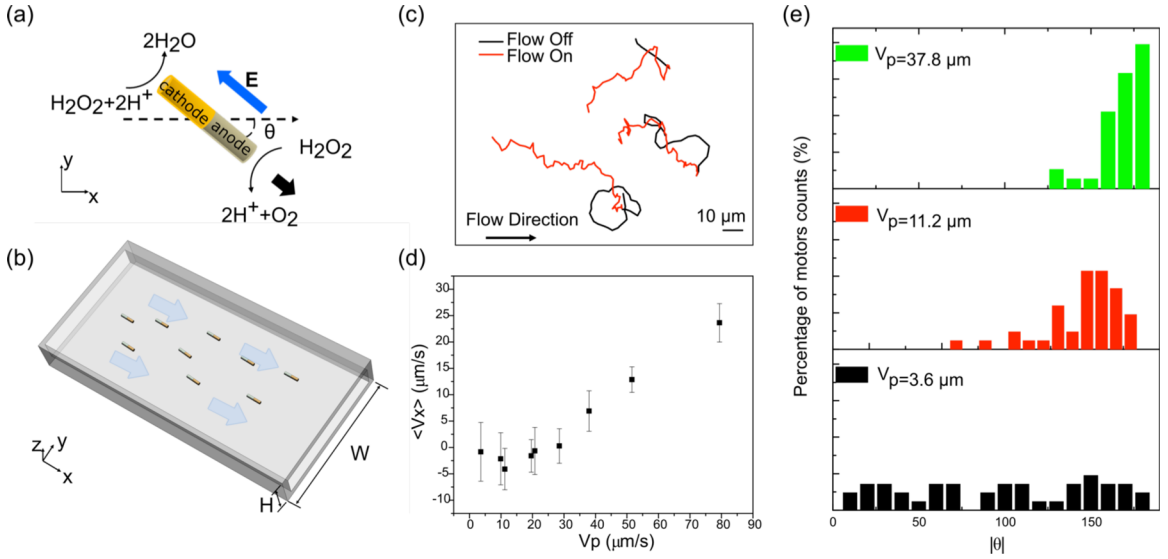

Figure 3. Orientation of chemically propelled bimetallic micromotors in shear flow. (a) Illustration of the bipolar electrochemical propulsion mechanism for catalytic bimetallic micromotors in H_2O_2; (b) schematic diagram of the experimental setup; (c) trajectories of bimetallic motors in a static fluid (black) and in shear flow (red); (d) relationship between motors' average velocity in the X direction $\langle V_x \rangle$ and the flow velocity V_p; (e) distribution of the angle θ measured at different flow velocities.

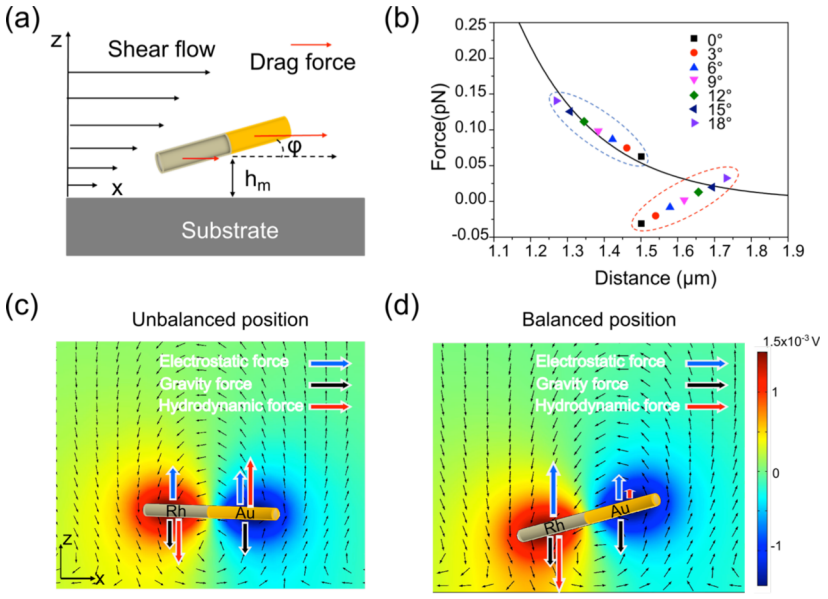

Figure 4. (a) Schematic illustration of the orientation process. The bimetallic motor forms an angle φ with the substrate. In shear flow, the tail end experiences a larger drag force than the head. (b) Comparison between the electric repulsion force F_e (black line) and the sum of the hydrodynamic force and gravity $-(F_h + F_g)$ on the motor's head (dots in the blue elliptical circle) and tail (dots in the red elliptical circle) at different values of φ, respectively. (c) Position of the motor if we balance only F_g and F_e, $\varphi = -2°$ with the heavier Au end closer to the substrate. In presence of H_2O_2, an electric potential difference (surface plot) develops around the micromotors and induces osmotic flow on both the rod and substrate surfaces. We plot the osmotic flow caused by the substrate (normalized arrows) as a counterclockwise flow that forms under the micromotor. (d) Balance position of the micromotor when we consider F_g, F_e, and the osmotic flow-induced hydrodynamic force, F_h. The resulting tilt angle is $\varphi = 12-15°$.

not considered in our model, may be comparable with F_y near the pressure node and may balance it. Thus, the trajectory of micromotors is not exactly parallel to or overlapping with the pressure node line.

These experiments demonstrate that this simple SAW-based acoustofluidic device can simultaneously guide and propel micromotors, which move autonomously near the bottom surface of the capillary. The device provides a reliable platform for systemically investigating the near-surface behavior of bimetallic micromotors in chemical−acoustic hybrid fields. In addition, it also offers an approach for orientation of autonomous motion along the capillary axis. Precise guidance of individual micromotors in arbitrary directions should be possible by using a more sophisticated channel or IDT design. However, collectively directing micromotors is still challenging because of their bidirectional orientations.

Orientation of Bimetallic Micromotors in H_2O_2. Unlike the bidirectional orientations observed in the acoustic field, we

DOI: 10.1021/acsnano.7b06107
ACS Nano 2017, 11, 10591−10598

found that bimetallic micromotors could be collectively oriented in one direction in H_2O_2 solution by using shear flow. The bimetallic micromotors can even exhibit positive rheotaxis at a moderate shear flow. Bimetallic microrods were originally developed as catalytic micromotors. In H_2O_2 solution, a self-induced electric field is generated by the oxidation and reduction of H_2O_2, which occur at different rates on the surface of the two metallic segments. The electric field then induces electro-osmotic flow on the surface of the micromotors, which are typically negatively charged, and drives axial movement toward the anode end (Figure 3a).[46,47] Although chemical fuels have some drawbacks for biomedical studies, the localized electric field and chemical gradient can generate many interesting phenomena because of motor−motor and motor−boundary interactions.

To observe chemically driven orientation and rheotaxis, we used a rectangular glass capillary (W = 2 mm, H = 200 μm, Figure 3b) to provide the shear flow environment. A large width-to-height ratio (W/H = 10) capillary was used so that we could consider the shear flow to exist only in the Z direction. Silicone microtubing was connected to the glass capillary to serve as the inlet and outlet. The flow was generated by a siphon effect, and the velocity was controlled by changing the height difference between the inlet and outlet. Bimetallic micromotors were suspended in 5% (v/v) H_2O_2 solution. Silica particles (2 μm in diameter) were added to the solution as tracer particles, and the flow velocity was detected by the velocity of the passive particles, V_p.

In the absence of the flow (V_p = 0 μm/s), the Au−Rh micromotors were axially propelled near the bottom surface in random directions. When flow was introduced along the X direction, the micromotors tended to turn their Rh ends against the flow direction and move upstream (Figure 3c and Movie S4). This positive rheotaxis behavior was quantitively analyzed by measuring the projection of the micromotors' velocity in the X direction, $\langle V_x \rangle = \langle V \cos \theta \rangle$. The bracket notation $\langle\ \rangle$ indicates an average value obtained from more than 40 independent observations. As the V_p increased from zero, $\langle V_x \rangle$ first decreased to a negative value because of the orientation effect, indicating collective positive rheotaxis. Then $\langle V_x \rangle$ started to increase and showed a linear relationship with V_p. When the flow rate exceeded the self-propulsion velocity, the micromotors migrated with the flow direction (positive $\langle V_x \rangle$) but with their Rh anode ends oriented against the flow. This is shown in Figure 3e as the narrowing of the distribution of θ angles with increasing V_p.

The orientation and rheotaxis effect of bimetallic micromotors in shear flow are similar to the behavior of self-diffusiophoretic hematite swimmers.[25] It is straightforward to show that the bimetallic micromotors are tilted at an angle φ to the bottom surface by a balance of forces that is developed during chemical self-propulsion. Thus, the tilted micromotors experience a larger drag force on their tail in shear flow and are aligned with the flow (Figure 4a). In our experiments, Ru−Au (Au end leading) and Rh−Au (Rh end leading) micromotors were investigated, respectively, and both demonstrated positive rheotaxis, regardless of which end was denser. In solutions without H_2O_2, the microrods followed the flow and no alignment was observed. The tilting does not result from simple gravitational effect.

We tested our hypothesis by using a modification of a 2D numerical model that was first developed to study the efficiency of catalytic bimetallic micromotors.[47] In the three-dimensional version of this model, a bimetallic rod (r = 150 nm, anode and cathode lengths both 1.5 μm) was placed near a solid wall (Figure S5). The half reactions of H_2O_2 were represented as positive and negative proton flux (j) normal to the anode and cathode surfaces, respectively. The electric field induced by the asymmetric distribution of protons around the micromotors was determined using the Poisson equation, and the fluid field was governed by the incompressible Navier−Stokes equation. We assumed that the electric double layer was infinitely thin so that the self-propulsion of the micromotor and the interaction between the micromotor and wall could be introduced by the electro-osmotic flow boundary on the surfaces of rod and wall. The electro-osmotic velocity, U_{eo}, is given by the Helmholtz−Smoluchowski equation:

$$U_{eo} = -\frac{\varepsilon_r \varepsilon_0 \xi}{\mu} E_t \tag{1}$$

where μ is the dynamic viscosity of the fluid, ε_0 is the permittivity of vacuum, ε_r is the relative permittivity of water, and E_t is the tangential electric field on the surface. The zeta potential of the bimetallic rod and glass capillary wall were approximated as ζ_m = −50 mV[48] and ζ_w = −50 mV,[49] respectively.

An important parameter for the simulation is the vertical distance between the micromotor and the wall, h_m (Figure 4a). We calculated this value by balancing the gravitational and electrostatic repulsion forces between the micromotor and the wall in DI water. We considered both the motor and the wall have constant surface potential, and the electrostatic repulsion force per unit length of the cylinder was calculated using eq 2:[50]

$$F = 2\sqrt{2\pi}\varepsilon_r \varepsilon_0 \kappa \sqrt{\kappa r_m}\left[\zeta_m \zeta_w \exp(-\kappa h_m) - \frac{1}{\sqrt{2}}\left(\zeta_w^2 + \zeta_m^2 \sqrt{\frac{r_m}{r_m + h_m}}\right)\exp(-2\kappa h_m)\right] \tag{2}$$

where

$$\kappa = \sqrt{\frac{2F^2 C_0}{\varepsilon_r \varepsilon_0 RT}} \tag{3}$$

where κ is the Debye−Hückel parameter, r_m is the radius of cylindrical micromotor, C_0 is the bulk concentration of protons, F is Faraday's constant, R is the universal gas constant, and T is the temperature, 293.15 K. For Au−Rh micromotors, h_m = 1.7 μm was obtained and a small tilt angle ($\varphi \approx -2°$) arises from the density difference between the two metals (Figure 4c, the Au end is closer to the wall). The van der Waals force between the cylinder and the wall was neglected because of the large h_m value obtained.

In addition to the electro-osmotic flow on the surface of the motor, the self-induced electric field also drives osmotic flow on the surface of the wall. A counterclockwise flow is generated beneath the micromotors (Figure 4c), which is consistent with a recent study.[51] The flow exerts hydrodynamic forces in opposite directions on the anode and cathode. The forces were calculated by integrating the Z direction total stress over the anode and cathode surfaces.

$$F_h = -\iint \tau \mathrm{d}s = -\iint (\tau_v - p\mathrm{d}z)\mathrm{d}s \tag{4}$$

DOI: 10.1021/acsnano.7b06107
ACS Nano 2017, 11, 10591−10598

where τ_v is the viscous stress, p is the fluid pressure, and dz is the unit mesh size in the Z direction. As a result, the motor will rotate around the Y axis and reach a new static position (Figure 4d).

In Figure 4b, the sum of the hydrodynamic and gravitational forces $-(F_g + F_h)$ on the anode (in the blue dashed ellipse) and cathode (in the red dashed ellipse) is compared with the electrostatic repulsion force F_e as φ is increased from 0 to 18°. This model indicates that a new force balance is reached when $\varphi \approx 12-15°$ (Rh end is closer to the wall). The hydrodynamic flow also brings the center of the micromotor slightly closer to the wall (h_m = 1.5 μm). The positive rheotaxis of bimetallic micromotors in shear flow can be successfully explained by the direction of this tilt angle φ. It is worth noting that we consider the zeta potential of bimetallic micromotors to be constant and uniform around the motors. In fact, the local pH change around the anode and cathode during the decomposition of H_2O_2 may cause the zeta potential to increase on the anode and decrease on the cathode, resulting in a larger φ than the value calculated here.

Collective Rheotaxis and Propulsion of Bimetallic Micromotors Using Hybrid Power. Whereas chemically powered bimetallic micromotors do exhibit positive rheotaxis, their collective upstream migration is inefficient. There is a trade-off between the orientation of the micromotors and their actual velocity relative to the capillary wall. A fast shear flow can overcome the Brownian rotation and align the cylindrical microrods well, but that process compromises their actual velocity. The acoustofluidic device is more powerful in terms of direction control and propulsion speed, but it cannot achieve unidirectional motion for collections of micromotors in flows. Here, we combine the chemical orientation and acoustic bidirectional propulsion effects by adding H_2O_2 to the acoustofluidic device. As shown in Movie S5, at a relatively low concentration H_2O_2 (2% v/v), the Rh−Au micromotors are oriented at $90° \leq |\theta| \leq 180°$, and their self-propulsion is almost quenched by the flow. When we apply the SAW (5 V), the majority of the micromotors lock their direction in $|\theta| = 180°$ and travel upstream. The trajectories of multiple micromotors over 3 s is shown in Figure 5a. Compared to the trajectories shown in Figure 4c, the bimetallic micromotors are oriented and propelled much more effectively in straight paths.

Another advantage of the hybrid-powered bimetallic micromotors is the ability to choose the direction of rheotaxis depending on the composition. For example, Ru−Au micromotors are propelled with their Au end (anode) leading in H_2O_2 but with their Ru end (lower density) leading in acoustic fields.[32] When we use Ru−Au micromotors to conduct the same experiment, they collectively move with the flow direction when the SAW is on (Figure 5b and Movie S6); that is, they exhibit negative rheotaxis. In this experiment, the micromotors are randomly distributed in the channel before the application of the SAW. When the SAW is applied, the Y direction acoustic force on micromotors that are far from the pressure node is not negligible. The micromotors move toward the pressure node as they are propelled acoustically and oriented chemically in the flow.

Whereas we have used Au−Rh and Au−Ru micromotors for this initial demonstration, any combination of bimetallic micromotors that have lighter anode ends should able to show enhanced positive rheotaxis with combined chemical and acoustic propulsion. For example, bimetallic Pd−Au, Rh−Pt, Ni−Au, and Ag−Au all move with the lighter end leading in H_2O_2 solutions,[46] and their movement should thus mimic that of Rh−Au. Si−Au photochemical motors[52] and Ag−Pt bimetallic micromotors that are chemically propelled in halogen solutions[53] also have lighter anode ends. Conversely, bimetallic micromotors such as Pt−Ru and Pt−Pd that have heavier anode ends should exhibit negative rheotaxis. Because shape effects dominate the direction of acoustic propulsion in the absence of significant density differences,[32] bimetallic Pt−Au rods should show positive or negative rheotaxis with acoustic in H_2O_2 depending on which end is concave. Furthermore, because the chemical and acoustic propulsion mechanisms are not limited to bimetallic micromotors, the hybrid strategy for collectively directing micromotors in response to shear flow might also be applicable to other designs of micromotors, including micromotors based on biodegradable materials.

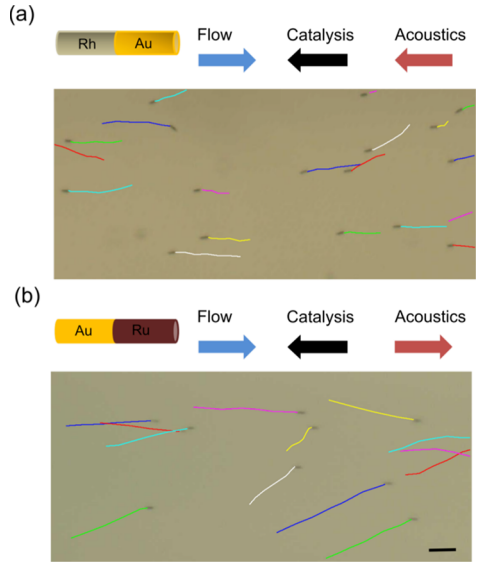

Figure 5. Directional collective motion of bimetallic micromotors. (a) For Rh−Au micromotors, the direction of their axial motion in the chemical and acoustic fields is the same. In the chemical−acoustic hybrid field, these micromotors exhibit positive rheotaxis. Trajectories over 3 s are plotted. (b) For Ru−Au micromotors, the direction of their axial motion in chemical and acoustic fields is opposite, and acoustic propulsion dominates the axial motion. Collective negative rheotaxis is demonstrated (trajectories over 3 s). The scale bar is 10 μm.

CONCLUSIONS

We have developed a hybrid strategy for bimetallic micromotors that enables them to mimic the rheotaxis behaviors of their natural counterparts, such as spermatozoa. Hydrodynamic force, chemical catalysis, and acoustic force are involved in this strategy, and they work in concert to achieve either positive or negative rheotaxis and fast propulsion. An acoustofluidic device was developed for the integration of chemical propulsion and acoustic propulsion along the bottom wall of a glass capillary. The behavior of bimetallic micromotors in the acoustic field alone and in the chemical fuel alone was investigated, and interesting phenomena were observed. In the acoustic field alone, micromotors can be propelled near the surface, and the direction of autonomous motion is guided by the acoustic field pattern. In H_2O_2 solution, the bimetallic micromotors exhibit positive rheotaxis by the same mechanism previously demonstrated for hematite swimmers, which involves tilting

DOI: 10.1021/acsnano.7b06107
ACS Nano 2017, 11, 10591−10598

of the micromotor cylinder axis relative to the surface. Numerical simulations enable an estimate of the tilt angle that results from the balance of gravitational, electrostatic, and hydrodynamic forces between the micromotors and the surface. We combine the advantages of these two propulsion mechanisms and to achieve both positive and negative rheotaxis in the hybrid fields. The ability to mimic this natural phenomenon and collectively direct automonous motion of powerful bimetallic micromotors represents a step forward toward the practical applications of synthetic micromotors in biomedicine and other fields.

MATERIALS AND METHODS

Fabrication of Bimetallic Micromotors. The Ru−Au and Rh−Au bimetallic micromotors were fabricated by electrodeposition in anodic alumina membranes (AAO, purchased from Whatman Inc., 200 nm pore size). A thin layer of Ag (300 nm) was evaporated onto the back side of the AAO membrane to serve as the working electrode during electrodeposition. For the deposition of Ag, Au, and Rh, a two-electrode system was used with a Pt coil as the counter electrode. Approximately 10 μm of Ag was first deposited as a sacrificial layer. The constant deposition current for Au and Rh was −1.22 and −2.45 mA/cm^2, respectively. Fifteen minutes of Au deposition and 120 min of Rh deposition resulted in ∼1.5 μm long segments for each (Figure S6). The deposition of Ru was done in a three-electrode system with Ag/AgCl in 3 M NaCl as the reference electrode. A constant potential of −0.65 V was used, and 30 min of deposition led to ∼1.5 μm long Ru segments. After the electrodeposition, the membranes were washed in DI water and soaked in 8 M HNO_3 for 5 min to dissolve the silver layer, followed by dissolution of the membrane in 1 M NaOH for 1 h. Finally, the micromotors were collected by centrifugation and then sonicated and cleaned in DI water for later use.

Fabrication of the Acoustofluidic Device. IDTs were fabricated on a lithium niobate substrate (128° Y-cut, 1 mm thickness, purchased from Red Optronics, USA). The pattern of IDTs was first fabricated on the substrate by a photolithographic process, then two metal layers (Cr/Au, 5 nm/50 nm) were evaporated by e-beam evaporation to cover the pattern. The IDTs were designed to work from 3 to 7 MHz. A square cross section glass capillary (200 μm × 200 μm inner dimensions, 100 μm wall thickness, VitroCom, USA) was aligned parallel to the IDTs and bonded to the substrate by two pieces of 60 μm thick spacers (double-sided tape, Kikusui tape, Japan) at the ends of the capillary. UV epoxy (NOA 61, Norland Optical Adhesives, USA) was transferred by a needle tip to the center region of capillary to fill the 60 μm thick air gap between the capillary and the substrate. The UV epoxy was cured under UV light for 15 min and formed the coupling layer. The capillary ends connected to standard silicone tubing (0.3 mm inner diameter, HelixMark, USA) for solution injection. The rectangular capillary used for chemical orientation and rheotaxis study was also purchased from VitroCom, USA.

Experimental Setup and Data Analysis. The experiments were conducted with an Olympus BX60 light microscope. Videos were captured at 30 frames per second by a USB camera (Flea3, Flir Integrated Imaging Solutions Inc. Canada) mounted on the microscope. The acoustofluidic device was driven by a RF signal function generator (33120A, Agilent, USA). The recorded videos were analyzed by using open source software ImageJ (NIH, USA). The statistical results such as the average velocity and distribution of angles were based on more than 40 individual samples.

Chemicals and Particles. The 2 μm silica tracer particles for flow velocity tracking and 4 μm silica particles for acoustic cargo transport experiments were purchased from Sigma-Aldrich. H_2O_2 30% was purchased from Fisher Chemicals and diluted for use.

ASSOCIATED CONTENT

Supporting Information

The Supporting Information is available free of charge on the ACS Publications website at DOI: 10.1021/acsnano.7b06107.

Additional figures and details of the numerical simulations described in the text (PDF)

Movie S1: The forward and backward motion of single bimetallic micromotor in the acoustic field (AVI)

Movie S2: The opposite-direction movement of two bimetallic micromotors in the acoustic field (AVI)

Movie S3: The pickup and transport of particles by bimetallic micromotors in the acoustic field (AVI)

Movie S4: Positive rheotaxis and orientation of bimetallic micromotors in H_2O_2 solution (AVI)

Movie S5: High-efficiency positive rheotaxis of Rh−Au micromotors with combined acoustic and chemical propulsion (AVI)

Movie S6: Negative rheotaxis of Ru−Au micromotors with combined acoustic and chemical propulsion (AVI)

AUTHOR INFORMATION

Corresponding Author

*E-mail: tem5@psu.edu.

ORCID

Pengtao Xu: 0000-0002-4470-446X

Tony Jun Huang: 0000-0003-1205-3313

Thomas E. Mallouk: 0000-0003-4599-4208

Notes

The authors declare no competing financial interest.

ACKNOWLEDGMENTS

This work was supported by the National Science Foundation under MRSEC Grant No. DMR-1420620. We also acknowledge the Research Computing and Cyber Infrastructure Unit of Information Technology Services at The Pennsylvania State University for providing advanced computing resources and services that contributed to the research results reported in this article.

REFERENCES

(1) Paxton, W. F.; Kistler, K. C.; Olmeda, C. C.; Sen, A.; St. Angelo, S. K.; Cao, Y.; Mallouk, T. E.; Lammert, P. E.; Crespi, V. H. Catalytic Nanomotors: Autonomous Movement of Striped Nanorods. *J. Am. Chem. Soc.* **2004**, *126*, 13424−13431.

(2) Sanchez, S.; Soler, L.; Katuri, J. Chemically Powered Micro- and Nanomotors. *Angew. Chem., Int. Ed.* **2015**, *54*, 1414−1444.

(3) Xu, T.; Gao, W.; Xu, L. P.; Zhang, X.; Wang, S. Fuel-Free Synthetic Micro-/Nanomachines. *Adv. Mater.* **2017**, *29*, 1603250.

(4) Gao, W.; Wang, J. The Environmental Impact of Micro/Nanomachines: A Review. *ACS Nano* **2014**, *8*, 3170−3180.

(5) Wang, J.; Gao, W. Nano/Microscale Motors: Biomedical Opportunities and Challenges. *ACS Nano* **2012**, *6*, 5745−5751.

(6) Abdelmohsen, L. K. E. A.; Peng, F.; Tu, Y.; Wilson, D. A. Micro- and Nano-Motors for Biomedical Applications. *J. Mater. Chem. B* **2014**, *2*, 2395−2408.

(7) Chałupniak, A.; Morales-Narváez, E.; Merkoçi, A. Micro and Nanomotors in Diagnostics. *Adv. Drug Delivery Rev.* **2015**, *95*, 104−116.

(8) Palacci, J.; Sacanna, S.; Vatchinsky, A.; Chaikin, P. M.; Pine, D. J. Photoactivated Colloidal Dockers for Cargo Transportation. *J. Am. Chem. Soc.* **2013**, *135*, 15978−15981.

(9) Tottori, S.; Zhang, L.; Qiu, F.; Krawczyk, K. K.; Franco-Obregón, A.; Nelson, B. J. Magnetic Helical Micromachines: Fabrication, Controlled Swimming, and Cargo Transport. *Adv. Mater.* **2012**, *24*, 811−816.

(10) Chen, C.; Mou, F.; Xu, L.; Wang, S.; Guan, J.; Feng, Z.; Wang, Q.; Kong, L.; Li, W.; Wang, J.; Zhang, Q. Light-Steered Isotropic Semiconductor Micromotors. *Adv. Mater.* **2017**, *29*, 1603374.

DOI: 10.1021/acsnano.7b06107
ACS Nano 2017, 11, 10591−10598

(11) Garcia-Gradilla, V.; Orozco, J.; Sattayasamitsathit, S.; Soto, F.; Kuralay, F.; Pourazary, A.; Katzenberg, A.; Gao, W.; Shen, Y.; Wang, J. Functionalized Ultrasound-Propelled Magnetically Guided Nanomotors: Toward Practical Biomedical Applications. *ACS Nano* **2013**, *7*, 9232−9240.
(12) Dong, R.; Zhang, Q.; Gao, W.; Pei, A.; Ren, B. Highly Efficient Light-Driven TiO_2 − Au Janus Micromotors. *ACS Nano* **2016**, *10*, 839−844.
(13) Ahmed, S.; Wang, W.; Mair, L. O.; Fraleigh, R. D.; Li, S.; Castro, L. A.; Hoyos, M.; Huang, T. J.; Mallouk, T. E. Steering Acoustically Propelled Nanowire Motors toward Cells in a Biologically Compatible Environment Using Magnetic Fields. *Langmuir* **2013**, *29*, 16113−16118.
(14) Dai, B.; Wang, J.; Xiong, Z.; Zhan, X.; Dai, W.; Li, C.-C.; Feng, S.-P.; Tang, J. Programmable Artificial Phototactic Microswimmer. *Nat. Nanotechnol.* **2016**, *11*, 1087−1092.
(15) Soto, F.; Martin, A.; Ibsen, S.; Vaidyanathan, M.; Garcia-Gradilla, V.; Levin, Y.; Escarpa, A.; Esener, S. C.; Wang, J. Acoustic Microcannons: Toward Advanced Microballistics. *ACS Nano* **2016**, *10*, 1522−1528.
(16) Ismagilov, R. F.; Schwartz, A.; Bowden, N.; Whitesides, G. M. Autonomous Movement and Self-Assembly. *Angew. Chem., Int. Ed.* **2002**, *41*, 652−654.
(17) Ibele, M.; Mallouk, T. E.; Sen, A. Schooling Behavior of Light-Powered Autonomous Micromotors in Water. *Angew. Chem., Int. Ed.* **2009**, *48*, 3308−3312.
(18) Wang, W.; Duan, W.; Sen, A.; Mallouk, T. E. Catalytically Powered Dynamic Assembly of Rod-Shaped Nanomotors and Passive Tracer Particles. *Proc. Natl. Acad. Sci. U. S. A.* **2013**, *110*, 17744−17749.
(19) Solovev, A. A.; Sanchez, S.; Schmidt, O. G. Collective Behaviour of Self-Propelled Catalytic Micromotors. *Nanoscale* **2013**, *5*, 1284.
(20) Katuri, J.; Seo, K. D.; Kim, D. S.; Sánchez, S. Artificial Micro-Swimmers in Simulated Natural Environments. *Lab Chip* **2016**, *16*, 1101−1105.
(21) Bretherton, F.; Rothschild. Rheotaxis of Spermatozoa. *Proc. R. Soc. London B Biol. Sci.* **1961**, *153*, 490.
(22) Arnold, G. P. Rheotropism in Fishes. *Biol. Rev. Camb. Philos. Soc.* **1974**, *49*, 515−576.
(23) Marcos; Fu, H. C.; Powers, T. R.; Stocker, R. Bacterial Rheotaxis. *Proc. Natl. Acad. Sci. U. S. A.* **2012**, *109*, 4780−4785.
(24) Zhang, Z.; Liu, J.; Meriano, J.; Ru, C.; Xie, S.; Luo, J.; Sun, Y. Human Sperm Rheotaxis: A Passive Physical Process. *Sci. Rep.* **2016**, *6*, 23553.
(25) Palacci, J.; Sacanna, S.; Abramian, A.; Barral, J.; Hanson, K.; Grosberg, A. Y.; Pine, D. J.; Chaikin, P. M. Artificial Rheotaxis. *Sci. Adv.* **2015**, *1*, e1400214.
(26) Das, S.; Garg, A.; Campbell, A. I.; Howse, J.; Sen, A.; Velegol, D.; Golestanian, R.; Ebbens, S. J. Boundaries Can Steer Active Janus Spheres. *Nat. Commun.* **2015**, *6*, 8999.
(27) Simmchen, J.; Katuri, J.; Uspal, W. E.; Popescu, M. N.; Tasinkevych, M.; Sánchez, S. Topographical Pathways Guide Chemical Microswimmers. *Nat. Commun.* **2016**, *7*, 10598.
(28) Uspal, W. E.; Popescu, M. N.; Dietrich, S.; Tasinkevych, M. Rheotaxis of Spherical Active Particles near a Planar Wall. *Soft Matter* **2015**, *11*, 6613−6632.
(29) Jang, B.; Wang, W.; Wiget, S.; Petruska, A. J.; Chen, X.; Hu, C.; Hong, A.; Folio, D.; Ferreira, A.; Pané, S.; Nelson, B. J. Catalytic Locomotion of Core-Shell Nanowire Motors. *ACS Nano* **2016**, *10*, 9983−9991.
(30) Wang, W.; Castro, L. A.; Hoyos, M.; Mallouk, T. E. Autonomous Motion of Metallic Microrods Propelled by Ultrasound. *ACS Nano* **2012**, *6*, 6122−6132.
(31) Soto, F.; Wagner, G. L.; Garcia-Gradilla, V.; Gillespie, K. T.; Lakshmipathy, D. R.; Karshalev, E.; Angell, C.; Chen, Y.; Wang, J. Acoustically Propelled Nanoshells. *Nanoscale* **2016**, *8*, 17788−17793.
(32) Ahmed, S.; Wang, W.; Bai, L.; Gentekos, D. T.; Hoyos, M.; Mallouk, T. E. Density and Shape Effects in the Acoustic Propulsion of Bimetallic Nanorod Motors. *ACS Nano* **2016**, *10*, 4763−4769.
(33) Wang, W.; Duan, W.; Zhang, Z.; Sun, M.; Sen, A.; Mallouk, T. E. A Tale of Two Forces: Simultaneous Chemical and Acoustic Propulsion of Bimetallic Micromotors. *Chem. Commun.* **2015**, *51*, 1020−1023.
(34) Xu, T.; Soto, F.; Gao, W.; Dong, R.; Garcia-Gradilla, V.; Magaña, E.; Zhang, X.; Wang, J. Reversible Swarming and Separation of Self-Propelled Chemically Powered Nanomotors under Acoustic Fields. *J. Am. Chem. Soc.* **2015**, *137*, 2163−2166.
(35) Nadal, F.; Lauga, E. Asymmetric Steady Streaming as a Mechanism for Acoustic Propulsion of Rigid Bodies. Phys. *Phys. Fluids* **2014**, *26*, 082001.
(36) Collis, J. F.; Chakraborty, D.; Sader, J. E. Autonomous Propulsion of Nanorods Trapped in an Acoustic Field. *J. Fluid Mech.* **2017**, *825*, 29−48.
(37) Dual, J.; Hahn, P.; Leibacher, I.; Möller, D.; Schwarz, T.; Wang, J. Acoustofluidics 19: Ultrasonic Microrobotics in Cavities: Devices and Numerical Simulation. *Lab Chip* **2012**, *12*, 4010−4021.
(38) Evander, M.; Nilsson, J. Acoustofluidics 20: Applications in Acoustic Trapping. *Lab Chip* **2012**, *12*, 4667−4676.
(39) Ding, X.; Lin, S.-C. S.; Kiraly, B.; Yue, H.; Li, S.; Chiang, I.-K.; Shi, J.; Benkovic, S. J.; Huang, T. J. On-Chip Manipulation of Single Microparticles, Cells, and Organisms Using Surface Acoustic Waves. *Proc. Natl. Acad. Sci. U. S. A.* **2012**, *109*, 11105−11109.
(40) Chen, Y.; Nawaz, A. A.; Zhao, Y.; Huang, P.-H.; McCoy, J. P.; Levine, S. J.; Wang, L.; Huang, T. J. Standing Surface Acoustic Wave (SSAW)-Based Microfluidic Cytometer. *Lab Chip* **2014**, *14*, 916−923.
(41) Ren, L.; Chen, Y.; Li, P.; Mao, Z.; Huang, P.-H.; Rufo, J.; Guo, F.; Wang, L.; McCoy, J. P.; Levine, S. J.; Huang, T. J. A High-Throughput Acoustic Cell Sorter. *Lab Chip* **2015**, *15*, 3870−3879.
(42) Guo, F.; Mao, Z.; Chen, Y.; Xie, Z.; Lata, J. P.; Li, P.; Ren, L.; Liu, J.; Yang, J.; Dao, M.; Suresh, S.; Huang, T. J. Three-Dimensional Manipulation of Single Cells Using Surface Acoustic Waves. *Proc. Natl. Acad. Sci. U. S. A.* **2016**, *113*, 1522−1527.
(43) Yeo, L. Y.; Friend, J. R. Surface Acoustic Wave Microfluidics. *Annu. Rev. Fluid Mech.* **2014**, *46*, 379−406.
(44) Mao, Z.; Li, P.; Wu, M.; Bachman, H.; Mesyngier, N.; Guo, X.; Liu, S.; Costanzo, F.; Huang, T. J. Enriching Nanoparticles *via* Acoustofluidics. *ACS Nano* **2017**, *11*, 603−612.
(45) Gor'kov, L. P. On the Forces Acting on a Small Particle in an Acoustical Field in an Ideal Fluid. *Sov. Phys. Dokl.* **1962**, *6*, 773.
(46) Wang, Y.; Hernandez, R. M.; Bartlett, D. J.; Bingham, J. M.; Kline, T. R.; Sen, A.; Mallouk, T. E. Bipolar Electrochemical Mechanism for the Propulsion of Catalytic Nanomotors in Hydrogen Peroxide Solutions. *Langmuir* **2006**, *22*, 10451−10456.
(47) Pumera, M. Electrochemically Powered Self-Propelled Electrophoretic Nanosubmarines. *Nanoscale* **2010**, *2*, 1643.
(48) Dougherty, G. M.; Rose, K. A.; Tok, J. B.-H.; Pannu, S. S.; Chuang, F. Y. S.; Sha, M. Y.; Chakarova, G.; Penn, S. G. The Zeta Potential of Surface-Functionalized Metallic Nanorod Particles in Aqueous Solution. *Electrophoresis* **2008**, *29*, 1131−1139.
(49) Xu, G.; Zhang, J.; Song, G. Effect of Complexation on the Zeta Potential of Silica Powder. *Powder Technol.* **2003**, *134*, 218−222.
(50) Ohshima, H. Electrostatic Interaction between a Cylinder and a Planar Surface. *Colloid Polym. Sci.* **1999**, *277*, 563−569.
(51) Liu, C.; Zhou, C.; Wang, W.; Zhang, H. P. Bimetallic Microswimmers Speed Up in Confining Channels. *Phys. Rev. Lett.* **2016**, *117*, 198001.
(52) Zhou, D.; Li, Y. C.; Xu, P.; Ren, L.; Zhang, G.; Mallouk, T. E.; Li, L. Visible Light-Driven Si-Au Micromotors in Water and Organic Solvents. *Nanoscale* **2017**, *9*, 11434−11438.
(53) Wong, F.; Sen, A. Progress Towards Light-Harvesting Self-Electrophoretic Motors: Highly Efficient Bimetallic Nanomotors and Micropumps in Halogen Media. *ACS Nano* **2016**, *10*, 7172−7179.

DOI: 10.1021/acsnano.7b06107
ACS Nano 2017, 11, 10591−10598